RSC Advances

PAPER

View Article Online
View Journal | View Issue

Cite this: *RSC Adv.*, 2025, **15**, 31461

Synthesis and characterization of thiol-stabilized gold nanoparticles appended to bis(pyrazole) pyridine for fabrication of rectangular nano/microstripes and their spin crossover and SERS studies

Ajay kumar Botcha*[a] and Yemineni S. L. V. Narayana*[b]

We report the synthesis and characterization of thiol-stabilized gold nanoparticles (AuNPs), functionalized with bis(pyrazole)pyridine ligands (**L4** and **10**), and their subsequent assembly into rectangular nano/microstripes using a lithographically controlled wetting (LCW) technique. The resulting microstructured patterns, with widths of ~2 μm and heights of 150–200 μm, were employed to simultaneously explore spin crossover (SCO) behavior and surface-enhanced Raman scattering (SERS) properties. Compound **10** exhibited SCO behavior with a molar magnetic susceptibility (χT) of ~3.3 emu K mol^{-1} at 320 K. AuNPs of spherical, cubic, and triangular morphologies were synthesized and characterized by transmission electron microscopy (TEM), and their shape-dependent surface plasmon resonance (SPR) features were analyzed *via* UV-vis spectroscopy. Further characterization was done using ^{1}H NMR, Raman spectroscopy, and atomic force microscopy (AFM). These nanostructures enable to combine magnetic and plasmonic characteristics in a single device.

Received 16th July 2025
Accepted 21st August 2025

DOI: 10.1039/d5ra05105c

rsc.li/rsc-advances

Introduction

Nanomaterials, particularly gold nanoparticles (AuNPs), have attracted significant attention due to their unique physical and chemical properties, including localized surface plasmon resonance (LSPR), high surface-area-to-volume ratios, and versatile surface functionality.[1–5] The tunability of these properties through precise size, shape, and surface modifications renders AuNPs highly promising for a wide range of applications, such as magnetic, electrical, optical, photonic, catalysis and drug delivery to advanced sensing platforms.[6–15] Among the various strategies for stabilizing and functionalizing AuNPs, thiol-based ligands have emerged as one of the most effective methods due to the strong affinity between thiol groups and gold surfaces.[16–18] However, beyond easy stabilization, the incorporation of well-designed organic ligands enables the development of complex hybrid nanomaterials featuring tunable properties. Incorporating organic ligands such as bis(pyrazole)pyridine (bpp), a well-known tridentate nitrogen-donor ligand, offers an opportunity for creating multifunctional hybrid nanomaterials. These hybrid systems not only benefit from the optical and electronic features of AuNPs but also inherit the coordination flexibility and structural adaptability of bpp-type ligands, which are mainly useful in supramolecular chemistry and spin crossover (SCO) systems.[19–28] SCO materials that undergo spin transitions in response to temperature variations are particularly promising for applications in molecular memory devices, displays and sensors.[24,29,30] Room-temperature SCO ensures compatibility with conventional operating conditions in most electronic systems, avoiding the necessity for external thermal control. Moreover, the reversible switching between spin states offers potential for applications in memory storage, logic circuits, and thermally responsive nanodevices.[31,32] Integrating such ligands onto AuNP surfaces facilitates stimuli–responsive behavior, magnetic or electronic switching features and directional bonding capability into the hybrid system. The structural adaptability of bpp further enables precise modulation of interparticle spacing, orientation, and surface coverage, all of which are vital for regulating plasmonic interactions, SERS performance, and ensuring compatibility with biological or catalytic contexts. SERS has demonstrated strong potential in bioanalysis, environmental monitoring, food safety, materials science, and point-of-care diagnostics. However, challenges remain in achieving consistent signal, fluorescence interference, limited reproducibility of substrates and hot spots, stability, and complex data analysis.[33,34]

[a]*Senior Lecture, Sri Chatanya College, Gajuwaka, Chinagatyada, Vizag, Andhra Pradesh, 530016, India. E-mail: Akchemistry@gmail.com*

[b]*Assistant Professor, Department of Chemistry, School of Applied Sciences & Humanities, Vignan's Foundation for Science, Technology and Research, Vadlamudi, Guntur, India-522213. E-mail: slvnarayanay@gmail.com; drysn_chmstry@vignan.ac.in; Tel: +91 863 2344777*

In recent years, increasing effort has been devoted to fabricating nanoscale architectures with well-defined geometries, such as nano- and microstripes, for use in photonic, electronic, and sensing applications.[35–40] The controlled self-assembly of functionalized nanoparticles into ordered arrays provides a pathway for creating anisotropic structures with potential in device integration.[41–44] Additionally, the use of such nanostructures in spin crossover studies presents an opportunity to explore bistable magnetic behavior at the nanoscale, while their plasmonic properties open opportunities for enhancing surface-enhanced Raman scattering (SERS) signals.

In this study, we report the fabrication of two-dimensional (2D) rectangular microstripes composed of gold nanoparticles (AuNPs, compound **10**) for the simultaneous investigation of spin-crossover (SCO) behaviour and surface-enhanced Raman scattering (SERS) under external stimuli, in a one-pot system. The synthetic approach was based on established procedures to prepare ligands **L4** and AuNP-based material **10**. The morphology and size distribution of the AuNPs were confirmed by transmission electron microscopy (TEM) and high-resolution TEM (HRTEM). Comparative ^{1}H NMR spectra of **L3** and **L4** confirmed the successful binding of AuNPs to the sulfur atoms of the ligand molecule. The SCO properties of complexes **9** and **10** were studied across the temperature range of 320 K to 2.5 K, revealing clear temperature-dependent magnetic switching. Pure Fe(II) thiol complex **9** was further employed as a model analyte for SERS measurements using the AuNP matrix of complex **10**. The AuNPs efficiently functioned as the SERS-active substrate, with enhanced Raman signals ascribed to the generation of electromagnetic "hot spots" at interparticle junctions. The lithographic wetting technique used for the fabrication of the rectangular AuNP microstripes offers a promising approach for the combined exploration of SCO effects and SERS activity within a unified system.

Result and discussion

Synthetic scheme

A novel synthetic route was developed for the preparation of thiol-stabilized gold nanoparticles (AuNPs), **L4**, and their Fe(II) complex (**10**) (Scheme 1), starting from the low-cost precursor citrazinic acid. The conversion of citrazinic acid to 2,6-dichloroisonicotinic acid methyl ester and its subsequent transformation into intermediate **5** was carried out following reported procedure.[45] The attachment of dec-1-yn-1-ol to compound **5** was achieved *via* a Sonogashira cross-coupling reaction, yielding compound 6 in 90% yield. Compound **6** was then tosylated using tosyl chloride in the presence of triethylamine to afford compound 7 in 82% yield. Subsequent treatment of 7 with lithium bromide in acetone at room temperature furnished compound **8** in 73% yield. The bromo derivative **8** was finally converted into the thiol-functionalized ligand **L3** using thiourea and sodium hydroxide in an acetone/ethanol (1 : 1) mixture at 80 °C, resulting in a 65% yield. This thiol ligand (**L3**) served as both a capping and stabilizing agent for the synthesis of AuNPs. Thiol-capped AuNPs (**L4**) were prepared by reacting ligand **L3** with $HAuCl_4$ in the presence of tetraoctylammonium bromide (TOAB) as a phase-transfer catalyst and $NaBH_4$ as the reducing agent. After completion of the reaction, the crude product was extracted using a DCM/water mixture, and the purified AuNPs were isolated. The Fe(II) complex **9** was synthesized by reacting two equivalents of **L3** with one equivalent of $Fe(ClO_4)_2 \cdot H_2O$ in acetonitrile at 60 °C, yielding 92%. Finally, thiol-stabilized AuNPs appended with bis(pyrazolyl)pyridine-based Fe(II) complex (**10**) were obtained by the dropwise addition of a methanolic solution of $Fe(ClO_4)_2 \cdot H_2O$ to a solution of **L4** in a dichloromethane/methanol mixture (8 : 2, v/v). Complete characterization of all synthesized compounds shown in the SI.

^{1}H-NMR spectroscopy studies

^{1}H NMR spectroscopy is a well-established technique for probing the chemical environments of protons and detecting the influence of paramagnetic species.[46] In this study, ^{1}H NMR was employed to examine the effect of sulfur–gold (S–Au) coordination on the chemical shift values of the bis(pyrazolyl) pyridine (BPP) ligand. As shown in Fig. 1, a comparative analysis of the ^{1}H NMR spectra of compounds **L3** (free thiol ligand) and **L4** (thiol-stabilized AuNPs) revealed significant changes in chemical shift positions along with pronounced line broadening. In the aromatic region, the BPP proton signals in **L4** exhibited noticeable upfield shifts relative to those in **L3**, accompanied by considerable broadening of the peaks, consistent with perturbation of the electronic environment upon Au–S coordination.[47] Furthermore, in the spectrum of **L3**, the $-CH_2SH$, alkyne-linked $-CH_2$, and thiol (–SH) protons appeared at δ 2.69, 2.40, and 1.65 ppm, respectively.[48] Upon formation of **L4**, these signals were no longer distinguishable and instead merged into a broad set of peaks between δ 2.3 and 1.0 ppm, indicating an overall upfield shift and significant peak broadening. This broadening effect, particularly in the aliphatic region, can be attributed to the paramagnetic influence of the gold nanoparticle core. The observed changes in chemical shift values, disappearance of characteristic proton signals, and spectral broadening collectively support the successful coordination of the thiol ligand to the gold surface, confirming the formation of **L4**. Additional characterizations of **L4** and **10** shown in the SI.

Determination of composition of L3, L4, and 10

Thermogravimetric analysis (TGA) was employed to estimate the composition of **L3**, **L4**, and **10** (Fig. 2), as this technique enables quantification of organic and inorganic components based on their thermal stability. The TGA curve of the free thiol ligand **L3** showed a decomposition onset at around 200 °C, with major degradation occurring by approximately 470 °C, resulting in a total weight loss of ~80%, which is consistent with the organic nature of the compound. In contrast, **L4** exhibited a weight loss of approximately 30%, attributed to the decomposition of the organic thiol ligand, while the remaining 70% corresponded to the thermally stable gold nanoparticle (AuNP) core (Fig. 2). These values suggest a composition ratio of approximately 1 : 2 (ligand: Au by weight), which aligns well

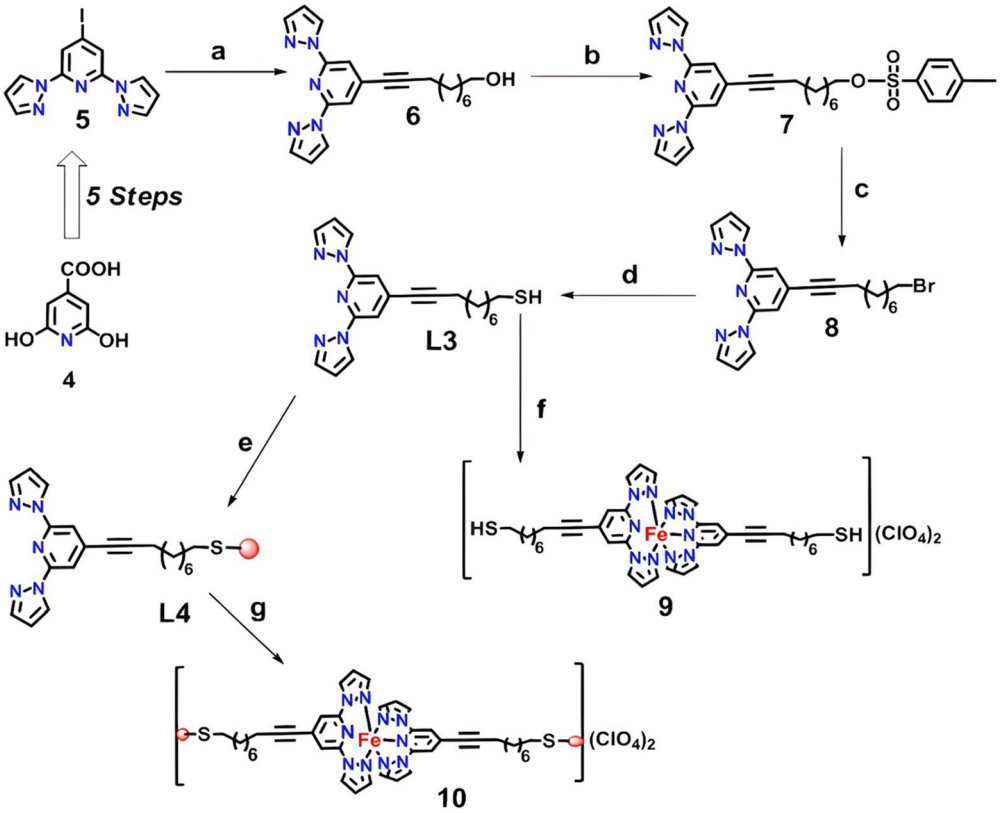

Scheme 1 Reagents and conditions: (a) 9-dec-yn-1-ol, CuI, PPh_3, $Pd(PPh_3)_2Cl_2$, NEt_3, 1,4 dioxane, 180 °C, 12 h. (b) Tosylchloride, DCM, NEt_3, RT, 4 h. (c) LiBr, acetone, RT, 2 h (d) thiourea, NaOH, EtOH, acetone, 80 °C, 26 h. (e) $HAuCl_4 \cdot 3H_2O$, TOAB, $NaBH_4$, H_2O, DCM, RT, 20 min. (f) $Fe(ClO_4) \cdot H_2O$, CH_3CN, 60 °C, 1 h (g) $Fe(ClO_4)_2 \cdot H_2O$, CH_3CN, DCM, RT, 15 min.

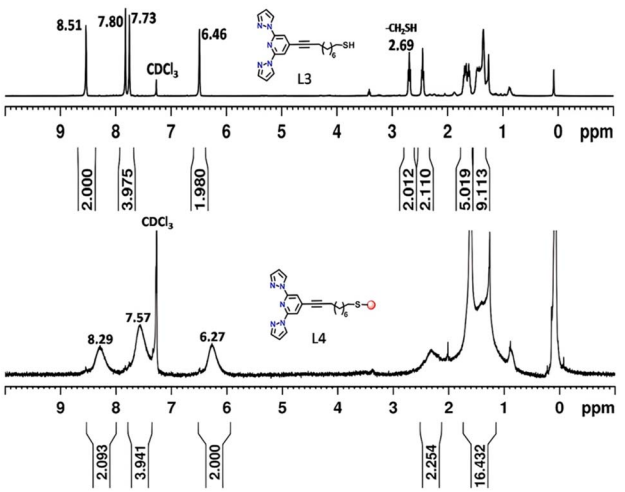

Fig. 1 Comparative ^{1}H NMR spectra of **L3** and **L4**.

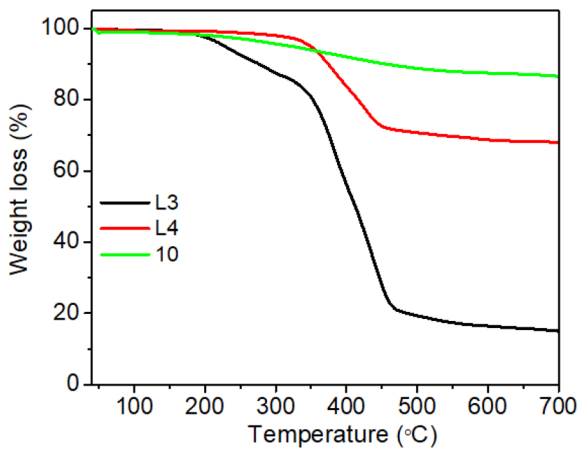

Fig. 2 TGA graphs of **L3**, **L4**, and **10**.

with the molar ratio of reagents used in the synthesis of **L4** (Fig. 3).

For compound **10**, the TGA data indicated a weight loss of ~10%, with the remaining 90% attributable to the AuNP content. This lower organic content is consistent with the formation of a coordination complex where the thiol-functionalized Fe(II)–BPP unit acts as a surface modifier on the AuNPs. These results confirm the successful formation of **L4** and **10**, and provide insight into their relative organic-to-metal content.

UV-visible spectroscopic studies of L3, L4 and 10

UV–Visible spectroscopy was employed to investigate the optical properties of **L3**, **L4**, and **10**, with the corresponding spectra presented in Fig. 3a. The absorption spectra of all three compounds exhibited characteristic bands at ~270 nm and in

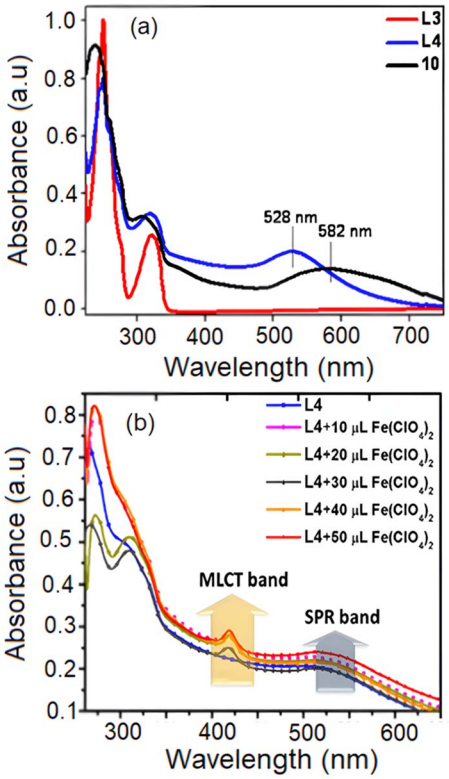

Fig. 3 (a) Absorbance of **L3**, **L4** and **10**, (b) titration of **L4** against $Fe(ClO_4)_2$.

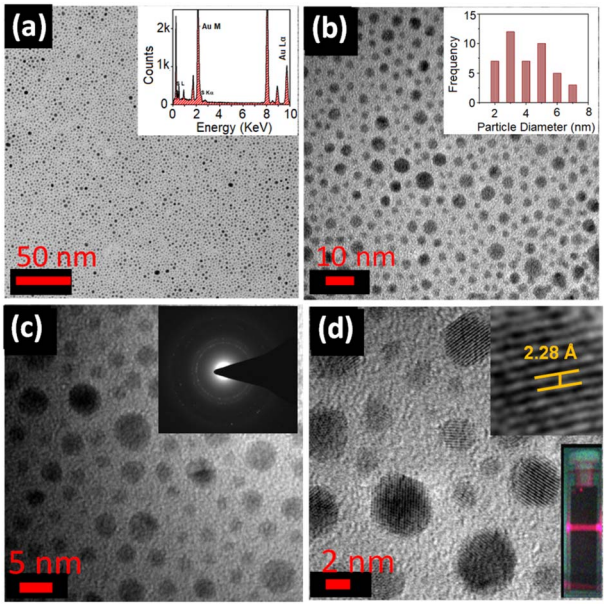

Fig. 4 (a–c) TEM images of Au NPs attached to **L4** with different magnifications, inset of (a) and (b) display the EDAX and histogram of spherical Au NPs of varying sizes; respectively. (c) The SAED pattern of Au NPs reveals the lattice spacing and grain boundaries. (d) The HRTEM image of spherical Au NPs and inset images shows inter planar spacing and Tyndall effect.

the 310–350 nm region, which are attributed to π–π* electronic transitions within the bis(pyrazolyl)pyridine (BPP) ligand. Gold nanoparticles typically show a surface plasmon resonance (SPR) band in the region of ~520 nm, with its exact position dependent on the size, shape, and dielectric environment of the particles. For the thiol-functionalized AuNPs (**L4**), a broad SPR band was observed around ~530 nm, indicating the successful formation of capped nanoparticles. Upon coordination with Fe(II) to form complex **10**, the SPR band further broadened and red-shifted to ~580 nm. This shift is attributed to aggregation of the AuNPs in the presence of Fe(II) counterions, and is indicative of changes in nanoparticle morphology and interparticle interactions. These spectral changes suggest a transformation in the shape and assembly of the AuNPs, which was further confirmed by transmission electron microscopy (TEM) analysis (Fig. 4).

To provide additional evidence for Fe–N coordination, UV-visible titration was performed by gradually adding a methanolic solution of $Fe(ClO_4)_2$ to a chloroform solution of **L4** (Fig. 3b). During the titration, a new absorption band emerged at ~420 nm, coexisting with the SPR band. This new band is assigned to a metal-to-ligand charge transfer (MLCT) transition, providing strong evidence for Fe–N bond formation between the BPP ligand and the Fe(II) ion.

Transmission electron microscope (TEM) studies of Au NPs (L4) and its Fe(II) complex (10)

Transmission electron microscopy (TEM) was employed to investigate the size and morphology of gold nanoparticles (AuNPs) stabilized by ligand **L3** (designated as **L4**) and its Fe(II) complex (**10**). For sample preparation, a dilute solution of thiol-capped AuNPs (**L4**) in dichloromethane (DCM) was prepared, and a drop of the resulting dispersion was drop-cast onto a carbon-coated copper grid. TEM images of **L4** (Fig. 4a–c) revealed predominantly spherical AuNPs with size distributions ranging from approximately 2.3 nm to 7 nm. The energy-dispersive X-ray (EDAX) spectrum (inset, Fig. 4a) confirmed the elemental composition of the nanoparticles as gold. The average particle size was determined by analyzing the TEM images using Image J software. A particle size histogram was generated by measuring the diameters of individual nanoparticles observed in Fig. 4b. The resulting histogram (inset of Fig. 4b) shows that the average particle diameter is approximately 4 nm. High-resolution transmission electron microscopy (HRTEM) images (Fig. 4c and d) displayed strong lattice fringes with an inter planar spacing of ~2.28 Å, consistent to the (111) planes of face-centered cubic (fcc) gold. The right inset in Fig. 4c displays the fringe contrast, where the atomic contrast may appear as bright or dark spots depending on imaging conditions. The selected area electron diffraction (SAED) pattern (Fig. 4c) further confirmed the polycrystalline nature of the AuNPs. Interestingly, TEM analysis of the Fe(II)-functionalized AuNPs (compound **10**) revealed a mixture of morphologies, including spherical, cubic, and triangular-shaped nanoparticles (Fig. 5a–d). The average size of the nanoparticles in **10** was notably larger than those observed for **L4**, which may be attributed to aggregation induced during complexation with $Fe(ClO_4)_2 \cdot H_2O$. The interplanar distances observed for the triangular and cubic nanoparticles were approximately 2.3 Å,

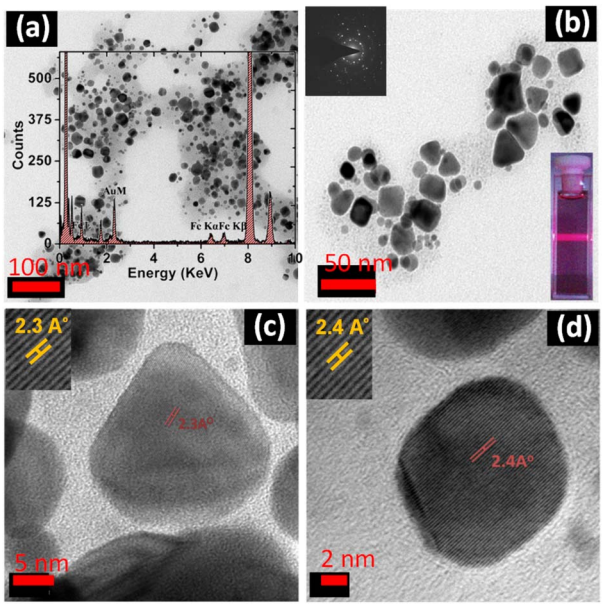

Fig. 5 (a) and (b) are TEM images of **10** in various magnifications displaying triangle, cubic Au NPs. Inset images of (a) and b) are shown the EDAX spectrum and SAED pattern, Tyndall effect of Au NPs. (c) and (d) are HRTEM images and inset images are shown inter planar spacing.

consistent with crystalline gold structures. The EDAX spectrum of **10** (inset, Fig. 5a) confirmed the presence of both Au and Fe, supporting the formation of the thiol-functionalized iron complex. The polycrystalline nature of these nanoparticles was further validated by the SAED pattern (inset, Fig. 5b) with the inset showing distinct grain boundaries and lattice fringes.

The measured lattice spacing matched well with the (111) planes of face-centered cubic (fcc) gold. Additionally, the selected area electron diffraction (SAED) pattern (Fig. 5b) showed clear concentric rings, which are a characteristic of gold nanoparticles that are polycrystalline. The colloidal solutions of **L4** and **10** exhibited deep brown and purple colors, respectively, characteristic of their SPR features. Additionally, a pronounced Tyndall effect was observed in the solution of **10** when irradiated with a 633 nm laser, as shown in the insets of Fig. 4d and 5d.

Magnetic properties of 9 and 10 Fe(II) complexes

The bulk magnetic behavior of the Fe(II) complexes **9** and **10** was investigated using temperature-dependent magnetic susceptibility measurements, as shown in Fig. 6. Both complexes exhibited spin crossover (SCO) behavior over the temperature range of 320 K to 2.5 K, albeit with notable differences in their thermal responses. For complex **9**, a pronounced and reversible SCO transition was observed (Fig. 6a). The molar magnetic susceptibility (χT) at 320 K was approximately 2.8 emu K mol^{-1} during the heating cycle and decreased to 0.28 emu K mol^{-1} upon cooling, indicating a complete transition from the high-spin (HS) to the low-spin (LS) state. The midpoint of the transition ($T_1/_2$) was found to be near room temperature, suggesting thermally accessible SCO under ambient conditions.

In contrast, complex **10**, in which the Fe(II) center is tethered to thiol-stabilized gold nanoparticles (AuNPs), displayed a more

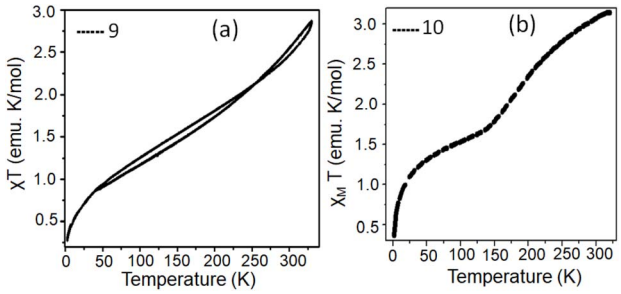

Fig. 6 χT *vs.* T plots of complex (a) **9** and (b) **10** respectively.

gradual and incomplete SCO transition (Fig. 6b). At 320 K, the χT value was ~3.3 emu K mol^{-1}, slightly higher than the expected value for a typical HS Fe(II) center ($S = 2$), which may be attributed to additional magnetic contributions from the AuNPs. Notably, at low temperatures, the χT value remained elevated (~1.5 emu K mol^{-1}), indicating a residual magnetic moment that could not be fully quenched by the SCO process. This residual χT value is ascribed to the presence of a small fraction of high-spin species that do not fully undergo spin crossover, even at low temperatures.[24]

This persistent magnetism at low temperature is likely due to the magnetic properties of the AuNPs themselves. While bulk gold is diamagnetic, gold nanoparticles have been reported to exhibit size- and surface-dependent magnetic behavior. One commonly proposed explanation is that lattice contraction at the nanoscale leads to shorter interatomic distances, enhancing d–d electronic interactions. However, in the present study, a comparison between Fig. 4 and 5 reveals an increase in lattice spacing relative to the bulk values, suggesting a deviation from this expected behavior. This observed lattice expansion may arise from several factors unique to the nanostructured or hybrid system, including surface ligand effects and interfacial strain. In the case of thiol-capped AuNPs, ligand-induced surface effects can further increase the number of holes in the 5d band of gold, resulting in the emergence of magnetic properties not observed in the bulk material. Thus, the observed residual magnetism in complex **10** is likely a combined effect of both incomplete spin crossover and intrinsic nanoparticle magnetism mediated by thiol–Au interactions.[49]

SERS study of 9 and 10

Surface plasmon resonance (SPR) in metal nanoparticles is highly sensitive to their size and shape. An increase in particle size typically enhances the SPR strength, which in turn improves the SERS enhancement factor. To achieve strong and reliable SERS signals, careful consideration of both the sample preparation and instrumental parameters is essential. In this study, SERS measurements were performed using a 633 nm He–Ne laser with a power output of 12 mW. The AuNPs in complex **10** displayed diverse morphologies, including triangular (18–25 nm), cubic (15–22 nm), and hexagonal (20–30 nm) particles—morphologies known to provide strong SERS activity due to their anisotropic nature and enhanced electromagnetic field

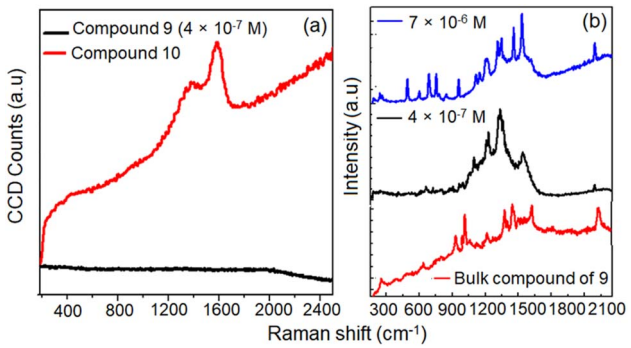

Fig. 7 (a) Raman spectra of **9** and **10** on thin film, (b) SERS spectra of complex **9** at different concentrations.

distribution. Hence, complex **10** was employed as a SERS-active substrate matrix. Initially, complex 9 (10 μL of a 4.0×10^{-7} M solution) was directly subjected to SERS measurements; however, no discernible Raman signals were observed (Fig. 7a). To enhance signal intensity, a thin film of complex **10** was first deposited on a silicon wafer. On this substrate, 10 μL of the same solution of complex **9** was drop-cast, and the solvent was permitted under ambient conditions. Under these modified conditions, distinct Raman signals were recorded for complex **9** in the spectral range of 1200–1700 cm^{-1} (Fig. 7b). However, at this concentration, the peaks were relatively weak and poorly resolved. To improve signal quality, the concentration of complex **9** was gradually increased. A clear enhancement in SERS intensity was observed at a concentration of 7.0×10^{-6} M. The recorded SERS spectrum closely resembled that of the bulk Raman spectrum of complex **9**, confirming the molecular identity (Fig. 7b). Notably, characteristic peaks observed in the bulk Raman spectrum at 2230 cm^{-1} (C≡C stretching) and 1620 cm^{-1} (C=C stretching) were shifted to 2190 cm^{-1} and 1534 cm^{-1}, respectively, when adsorbed onto the AuNP substrate of complex **10**. Additionally, new well-defined peaks emerged at 1309 cm^{-1}, 1112 cm^{-1}, 688 cm^{-1}, 490 cm^{-1}, and 243 cm^{-1}, suggesting enhanced molecular interactions between complex **9** and the AuNP surface. These results clearly demonstrate that the presence of anisotropic AuNPs in complex **10** is crucial for SERS enhancement, enabling the detection of low concentrations of analyte molecules such as complex **9**.

Fabrication of rectangle micro stripes by 10

As demonstrated in the previous SERS experiments, complex **9** exhibited enhanced Raman signals only in the presence of anisotropic AuNPs from complex **10**. This enhancement suggests that complex **10** can function as an effective plasmonic platform. It is well-established that the optical properties of

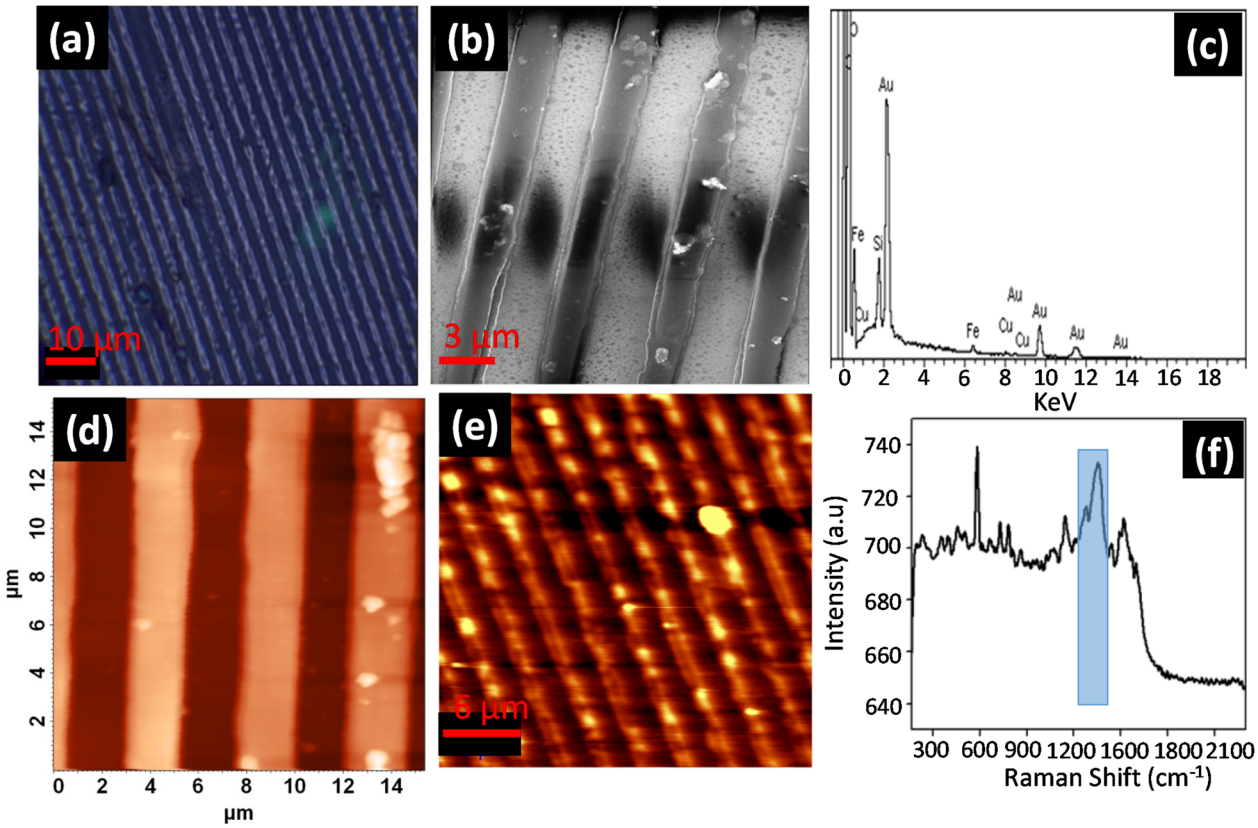

Fig. 8 (a) Confocal microscopy image of microstripes of **10**, (b) FESEM image of micro stripes of **10**, the red spot indicates EDS spectrum collected area, (c) EDS spectrum of **10** collected from micro stripes, in EDS spectrum shows Fe, Au, S elements are present on the microstripes. (d) AFM 2D-image of microstripes. (e) Laser confocal Raman microscopy 3D-image of microstripes. (f) Raman spectrum from microstripes composed of polymer **10**.

AuNPs can be significantly altered when they are organized into well-defined architectures, particularly through control of interparticle spacing. When nanoparticles are brought into close proximity, collective plasmonic coupling occurs, resulting in electromagnetic "hot spots" that amplify local fields—an essential feature for SERS applications. In the past literature, Au NPs were put in a desired pattern by using electron beam lithography in order to control distance between adjacent particles such that plasmonic propagation to be occur along the pattern, generating hot spots it's leading into study of surface enhance Raman scattering effect.[50] In the present complex **10** was lithographically patterned with PDMS.

Rectangular micro stripes of microstripes were produced by lithographically wetting technique (LCW) with PDMS mould.[51] The experiment setup for measuring SERS is shown in supporting information Fig. S20. The prepared micro patterns were analyzed by atomic force microscope (AFM) and field emission scanning electron microscope (FESEM) techniques. The AFM images revealed that the height and width of the rectangular stripes were approximately 150–200 nm and ~2 μm, respectively. These morphological features were consistent with the FESEM analysis. Energy-dispersive X-ray (EDAX) analysis further confirmed the presence of Fe, Au, and S elements within the patterned structures (Fig. 8c), validating the successful incorporation of complex **10** into the microstripes. The lithographically patterned microstripes of complex **10** were further subjected to Raman spectroscopic analysis, including both spectral acquisition and spatial Raman imaging. A distinct and intense Raman peak was observed at 1529 cm^{-1}, corresponding to the C=C stretching mode, indicative of surface-enhanced Raman scattering (SERS) arising from the plasmonic activity of the embedded AuNPs.

This peak at 1529 cm^{-1} was selected as a representative signal for Raman mapping of the rectangular microstripes over an area of 2 μm × 2 μm (Fig. 8e and f). Raman imaging was carried out using a 633 nm He–Ne laser with an integration time of 0.1 s. Multiple Raman spectra collected from various points on the microstripes exhibited significant spectral variations in intensity and signal profile, which is characteristic of SERS-active substrates. Such variation is attributed to the heterogeneous distribution of plasmonic hot spots within the patterned film, leading to localized enhancement effects.

Experimental section

Synthetic procedures

10-(2,6-Di(1*H*-pyrazol-1-yl)pyridine-4-yl)dec-9-yn-1-ol (6). 4-Iodo-2,6-di (1*H*-pyrazole-1-yl)pyridine (**5**) (0.317 g, 0.94 mmol), $Pd(PPh_3)_2Cl_2$ (0.032 g, 0.046 mmol), PPh_3(0.024 g, 0.0934 mmol), CuI (0.011 g, 0.062 mmol) were taken in a 100 mL two neck round bottom flask. To this solid mixture, high vacuum pump was applied through condenser for deoxynation. Subsequently dry triethylamine (15 mL), 1,4 dioxane (3 mL) were added slowly to the deoxynated solid mixture under N_2 atmosphere. After five minutes 9-dec-yn-1-ol (0.217 g, 1.41 mmol) was added and refluxed it for 8 hours under N_2 atmosphere at 80 °C. All the solvents were removed under reduced pressure through rotary evaporator and resultant crude product purified by column chromatography by using EtOAc : hexane (3 : 7). Finally, a pure compound **6** (90% yield) was obtained as white colour solid. ^{1}H-NMR (400 MHz, $CDCl_3$): δ = 8.54 (d, 2H), 7.83 (S, 2H), 7.75 (d, 2H), 6.49 (M, 2H), 3.66 (m, 2H), 2.46 (m, 2H), 1.6–1.3 (m, 2H) ppm. ^{13}C-NMR (200 MHz, $CDCl_3$): δ = 149.9, 142.4, 137.6, 128.4, 111.5, 108.0, 97.4, 62.5, 32.6, 29.2, 25.6, 19.4 ppm. FTIR (KBr disc; ν in cm^{-1}): 3393, 3155, 2930, 2848, 2237, 1739, 1610, 1552, 1521, 1462, 1396, 1261, 1205, 1116, 1039, 954, 935, 868, 790, 760, 723. LCMS analysis *m*/*z*: experimental value: 363.0, calculated value *m*/*z*: 363.46.

10-(2,6-Di(1*H*-pyrazol-1-yl)pyridine-4-yl)dec-9-ynyl-4-methylbezenesulphonate (7). To the suspension solution of **6** (0.3 g, 0.82 mmol) in DCM (15 mL) and NEt_3 (5 mL) solution, tosylchloride (0.314 g, 1.65 mmol) was added. The reaction mixture was stirred for 2 h at room temperature. Afterwards all the solvents were evaporated under reduced pressure and resultant black solid was purified by column chromatography with EtOAc/hexane (1 : 9), to obtain a colourless solid compound **7** (80%). ^{1}H-NMR (400 MHz, $CDCl_3$): δ = 8.5 (d, 2H), 7.8 (s, 2H), 7.75 (d, 2H), 7.72 (d, 2H), 7.3 (d, 2H), 6.46 (m, 2H), 4.0 (m, –CH2), 2.4 (m, 5H), 1.6 (m, 6H), 1.2 (m, 6H) ppm. ^{13}C-NMR (200 MHz, CDCl3): δ = 150.0, 144.6, 142.5, 129.8, 129.6, 128.9, 127.8, 125.2, 111.54, 108.06, 97.19, 64.5, 29.6, 28.8, 25.7, 21.6, 19.4 ppm. FTIR (KBr disc; ν in cm^{-1}): 3115, 2922, 2852, 2224, 1784, 1730, 1610, 1552, 1523, 1464, 1398, 1358, 1267, 1207, 1176, 1113, 1049, 939, 900, 864, 821, 761, 661, 625, 574, 551, 474. LCMS analysis *m*/*z*: experimental value: 518.14, calculated value: 517.64.

4-(10-Bromodec-ynyl)-2,6-di(1*H*-pyrazol-1-yl)pyridine (8). Compound **7** (0.13 g, 0.2511 mmol) was dissolved in dry acetone and lithium bromide (0.043 g, 0.502 mmol) was added to resultant solution. After 2 hours acetone has been removed by rotary evaporator under reduced pressure. Afterwards resultant mixture was extracted with DCM solvent in water. Evaporation organic layer (DCM) has produced white colour compound **8**, yield was found to be 75%. ^{1}H-NMR (400 MHz, $CDCl_3$): δ = 8.48 (d, 2H), 7.78 (s, 2H), 7.71 (d, 2H), 6.4 (m, 2H), 3.39 (m, $-CH_2$), 2.43 (m, $-CH_2$), 1.8 (m, $-CH_2$), 1.58 (m, $-CH_2$), 1.43 (m, 4H), 1.27 (m, 4H) ppm. ^{13}C-NMR (200 MHz, $CDCl_3$): δ = 150.0, 142.3, 137.5, 127.0, 111.5, 108.0, 97.1, 78.4, 32.08, 28.9, 19.4 ppm. FTIR (KBr disc; ν in cm^{-1}): 3150, 3101, 2930, 2856, 2237, 1734, 1610, 1552, 1521, 1462, 1396, 1259, 1205, 1111, 1039, 954, 868, 790, 760, 626. LCMS analysis *m*/*z*: experimental value: 426.0, calculated value: 426.35.

10-(2,6-Di(1*H*-pyrazole-1-yl)pyridine-4-yl)dec-9-yne-1-thiol (L3). Compound **8** (0.100 g, 0.235 mmol) was dissolved in 1 : 1 acetone/ethanol solution in a 100 mL round bottom flask. Thiourea (0.021, 0.282 mmol) was added to this solution and left it for reflux at 80 °C about 24 hours. Then all the solvents were evaporated and obtained crude was dispersed in NaOH (0.009 g, 0.235 mmol) solution. This solution was refluxed for $1\frac{1}{2}$ hour and cooled it to room temperature. Then obtained solid was purified by EtOAc/hexane (1 : 9) solution, consequently, 50% of gel type colorless compound was observed. ^{1}H-NMR (400 MHz, $CDCl_3$): δ = 8.51 (d, 2H), 7.80 (s, 2H), 7.73 (d, 1H), 6.46 (m, 2H), 2.7 (m, -SCH2), 2.45 (m, 2H), 1.6 (m, 2H), 1.69 (m, 2H), 1.4

(m, 10H) ppm. ^{13}C-NMR (200 MHz, $CDCl_3$): δ = 150.0, 142.4, 137.6, 127.0, 111.6, 108.0, 97.0, 78.3, 39.1, 29.7, 29.2, 29.1, 29.0, 28.8, 28.5, 28.2, 19.4 ppm. FTIR (KBr disc; ν in cm^{-1}): 3158, 3112, 2919, 2848, 2358, 2339, 2225, 1739, 1608, 1550, 1459, 1394, 1263, 1205, 1110, 1031, 956, 933, 862, 771. LCMS analysis *m*/*z*: experimental value: 380.10, calculated value: 379.21.

Synthesis of pure thiol complex (9). Ligand **L3** (0.050 g, 0.132 mmol) was first dissolved in 15 mL of acetonitrile solvent in 100 mL round bottom flask and Fe $(ClO_4)_2.6H_2O$ (0.0168 g, 0.066 mmol) was added to this resultant ligand solution followed by stirring at 60 °C about 1 hour. Then solution was allowed to cool till it reaches room temperature, further, it was poured in diisopropylether to achieve pure brown colour precipitate of thiol complex **2**, yield was calculated to be 60%. FTIR (KBr disc; ν in cm^{-1}): 3140, 3112, 2925, 2700, 2400, 2339, 2225, 1739, 1600, 1550, 1403, 1394, 1255, 1220, 1111, 1031, 940, 920, 862, 680. Raman (neat pellet; cm^{-1}): 2229, 1638 (C═C), 1452, 1384, 1215, 1021, 936, 801, 632, 479, 370, 243.

Synthesis of Au NPs capped by L3 (L4). $HAuCl_3 \cdot 3H_2O$ (0.186 g, 0.474 mmol) was taken in 2 mL millipore water in 100 mL round bottom flask. Tetraoctylammonium bromide (TOAB) (0.518 g, 0.948 mmol) in DCM (2 mL) and ligand **L3** (0.090 g, 0.237 mmol) in 2 mL DCM were introduced to this solution. Resultant mixture was stirred for 10 minutes at room temperature. Finally, freshly prepared sodium borohydride (0.143 g, 3.792 mmol) solution in 2 mL millipore water was added drop by drop. Immediately a yellow colour solution has turned into dark brown which indicates that formation of Au NPs capped by thiol ligand **L3**. The resultant solution was left it for stirring for 15 minutes at RT and then organic layer was separated and rest of aqueous layer washed with washed with extra amount of DCM solvent. Afterwards, all organic fractions were mixed and evaporated to get dark brown color solid with excess amount of TOAB. Excess amount of TOAB has been removed by washing with methanol solvent to achieve thiol capped Au NPs (**L4**) in pure form and it was characterized by UV-visible spectroscopy, ^{1}H-NMR and TEM. ^{1}H-NMR (400 MHz, $CDCl_3$): δ = 8.29 (d, 2H), 7.57 (s, 4H), 6.27 (d, 2H), 2.32 (m, 2H), 1.1–1.8 (m, 16H) ppm. UV-visible (λ_{abs} max in nm): 520, 334, 270. FTIR (KBr disc; ν in cm^{-1}): 2921, 2854, 2337, 2225, 1623, 1556, 1523, 1457, 1405, 1340, 1268, 1214. Raman (neat pellet; cm^{-1}): 2239, 1632 (C═C), 1555, 1529, 1497, 1458, 1408, 1386, 1216, 1123, 1061, 1016, 929, 634, 253.

Synthesis Fe(II) complex of L4 (10). Initially ligand **L4** (0.05 g) was dissolved in 3 : 7 mixtures of DCM and acetonitrile in 100 mL round bottom flask. To this solution, very dilute solution of $Fe(ClO_4)_2 \cdot H_2O$ was added slowly drop by drop and solution was left it for about 20 minutes at room temperature. Insoluble complex **10** was settled as black precipitate which was separated by decanting solvent without losing compound. The black solid was further washed with DCM and methanol to remove excess of ligand and metal ion. Now pure complex was characterized by ^{1}HNMR, UV-visible spectroscopy and TEM. ^{1}H-NMR (400 MHz, $CDCl_3$): δ = 8.5, 7.65, 6.40, 2.4, 17–0.8 ppm. UV-visible (λ_{abs} max in nm): ~500–600, 304, 270. FTIR (KBr disc; ν in cm^{-1}): 2931, 2854, 1627, 1529, 1452, 1403, 1263, 1230, 1099, 968, 860, 767. Raman (neat pellet; cm^{-1}): 1529, 1452, 1346, 1308, 1205, 1111, 960, 755, 685, 593, 493.

Time taken to prepare compounds and necessary precautions

We spent approximately two months completing the synthesis work described in this study. Particular care was required during the preparation of compounds **7** and **L3**. In the synthesis of compound **7**, tosyl chloride was used, which is known to cause eye and skin irritation. Therefore, appropriate safety precautions, such as working in a fume hood and wearing protective equipment, were strictly followed. Compound **L3** contains a thiol group, which is associated with a strong and unpleasant odor. To minimize exposure, handling was done in a well-ventilated area using a suitable mask. Additionally, compound **L4** exhibited limited stability in solution; hence, it was used immediately for the synthesis of the corresponding iron complex to avoid degradation.

Instrumentation details

^{1}H and ^{13}C NMR spectroscopy data were recorded on a Bruker DPX 500 MHz spectrometer with solvent proton as an internal standard ($CDCl_3$-*d*1 = 7.26 ppm). LC mass spectrometry was performed on Shimadzu LCMS-2010A mass spectrometer. ESI-Mass spectrometry was performed on Bruker maXis ESI-TOF spectrometer. IR spectra were recorded on a JASCO FT/IR-5300 or Nicolet 5700 FT-IR instrument equipped with ATR attachment. Elemental analysis was recorded on a C H N analysis Thermo Finnigan Flash EA 1112 analyzer instrument. UV-visible absorption spectra were recorded on a spectrophotometer Cary-100, Varian. For thin-layer chromatography (TLC), silica gel plates Merck 60 F254 were used and compounds were visualized by irradiation with UV light.

Bulk magnetic studies

The temperature dependent magnetic susceptibility of complex I in the powder state was measured on a Quantum Design vibrating sample magnetometer (VSM-SQUID) setup in the temperature range of 340 ↔ 2 K at continuous cooling (↓) and heating (↑) cycles with an applied direct current (DC) magnetic field of 0.5 T. Heating and cooling rate of the sample was kept at a 10 K interval in sweep mode.

Electron microscopy studies

Size and morphology of the micro structures were examined by using a Philips XL30 ESEM Scanning Electron Microscope using a beam voltage of 20 kV. TEM measurement was carried out on Tecnai G2 FEI F12 instrument at an accelerating voltage of 120 kV. Carbon coated TEM grids (200 Mesh Type B) were purchased from Ted Pella Inc. U.S.A.

Method for patterning

Micro patterning of complex 10 was carried out by drop casting 20 μL of a 2 mg mL^{-1} solution of complex I in acetonitrile

(Aldrich, ≥99% purity) on glass substrate. The substrate was cleaned by sonication for 2 min in electronic-grade water (Milli-Q-pure quality), 2 min in acetone (Aldrich chromatography quality), and then with 2-propanol (Aldrich spectroscopic-grade quality). Before micro patterning the solution of compound I was filtered through a Whatman filter paper.

Poly(dimethylsiloxane) (PDMS) stamps for lithography

Elastomeric PDMS (Sylgard 184 Down Corning) stamps were prepared by replica molding of a structured master (NTMDT AFM test gratings-TGZ3). The curing process was carried out at 60 °C for 6 h. Once cured, the replica was carefully peeled-off from the master and used as such for micropatterning techniques.

Atomic force microscopy (AFM). AFM imaging was carried out on NT-MDT Model Solver Pro M microscope using a class 2R laser of 650 nm wavelength having maximum output of 1 mW. All calculations and image processing was carried out by a software NOVA 1.0.26.1443 provided by the manufacturer. The images were recorded in a semicontact mode using a noncontact silicon cantilever (NSG10-DLC) tip purchased from NT-MDT, Moscow. The dimension of the tip is as follows: cantilever length = 100 (±5) μm, cantilever width 35 (±5) μm, and cantilever thickness = 1.7–2.3 μm, resonate frequency = 190–325 kHz, force constant = 5.5–22.5 N m^{-1}, chip size = 3.6 × 1.6 × 0.4 mm, reflective side = Au, tip height = 10–20 μm, tip curvature radius = 1–3 nm, and aspect ratio 3 : 1–5 : 1.

Confocal Raman micro spectroscopy studies. Raman spectra of the samples were recorded on a WI-Tec confocal Raman spectrometer equipped with a Peltier-cooled CCD detector. Using a 600 grooves/mm grating BLZ = 500 nm, the accumulation time was typically 10 s and integration time was typically 2.0000 s. 10 accumulations was executed for attaining a single spectrum. For imaging the integration time was typically 2.000 s, keeping in mind that the *x* or *y* resolution is ∼250 nm four points per line and four line an image was captured to visualize a 1 μm × 1 μm area. A He–Ne laser with a wavelength of 633 nm assisted as the excitation source for the Raman scattering. All measurements were done at ambient conditions.

SERS experiments. Experiments were conducted using complex **10** coated on silicon wafer, as the SERS substrate. Complex **9** was used as the analyte molecule; 10 μL of 0.4 μM solution of complex **9** in methanol was spread uniformly on the substrate and dried under ambient atmosphere. A WITec model Alpha 300 R Raman microscope was used for recording the Raman spectra, with 0.5 s integration time and 10 accumulations, through a 100× aperture (NA = 0.89). A 633 nm He–Ne laser with 12 m Watt power was used as the excitation source. The laser intensity was maintained constant in all measurements; a 100 μm detecting fiber was used to collect the spectra. A Raman spectrum for the bulk material used as the reference was recorded using a small amount of complex **9** powdered placed on the Si wafer.

Conclusions

We have successfully synthesized thiol-stabilized Au NPs (**L4** and **10**) and fabricated a switchable plasmonic memory device based on **10** using a lithographic wetting method. Spin-crossover (SCO) and surface-enhanced Raman scattering (SERS) studies have been conducted on the device, offering valuable insights for future investigations into SCO behavior and SERS responses under light irradiation.

Conflicts of interest

There are no conflicts of interest to declare.

Data availability

The data supporting this article have been included as part of the SI. See DOI: https://doi.org/10.1039/d5ra05105c.

Acknowledgements

Infrastructure support from the Centre for Nanotechnology for TEM and Raman, FESEM facility (School of Chemistry) at the University of Hyderabad are acknowledged with gratitude. We thank Prof. R. Chandrasekar for discussion and experimental clarification. YSLVN thank Vignan's Foundation for Science, Technology and Research (VFSTR) for providing the infrastructure to conduct the research work.

References

1 M. C. Daniel and D. A. struc, *Chem. Rev.*, 2004, **104**, 293–346.
2 K. Kant, R. Beeram, Y. Cao, *et al.*, *Nanoscale Horiz.*, 2024, **9**, 2085–2166.
3 H. Duman, E. Akdaşçi, F. Eker, M. Bechelany and S. Karav, *Nanomaterials*, 2024, **14**, 1805.
4 P. Si, N. Razmi, O. Nur, S. Solanki, C. M. Pandey, R. K. Gupta, B. D. Malhotra, M. Willander and A. de la Zerda, *Nanoscale Adv.*, 2021, **3**, 2679–2698.
5 F. Tian, F. Bonnier, A. Casey, A. E. Shanahan and H. J. Byrne, *Anal. Methods*, 2014, **6**, 9116.
6 Y. Wang and N. Herron, *Science*, 1996, **273**, 632.
7 M. Nirmal, B. O. Dabbousi, M. G. Bawendi, J. J. Macklin, J. K. Trautman, T. D. Harris and T. D. L. E. Brus, *Nature*, 1996, **383**, 802.
8 N. Toshima and T. Yonezawa, *New J. Chem.*, 1998, **22**, 1179.
9 M. P. Pileni, *New J. Chem.*, 1998, **22**, 693–702.
10 P. Gomez-Romero, *Adv. Mater.*, 2001, **13**, 163.
11 J. J. Hickman, D. Ofer, P. E. Laibinis, G. M. Whitesides and M. S. Wrighton, *Science*, 1991, **252**, 688.
12 S. Chen, R. S. Ingram, M. J. Hostetler, J. J. Pietron, R. W. Murray, T. G. Schaaff, J. T. Khoury, M. W. Alvarez and R. L Whetten, *Science*, 1998, **280**, 2098.
13 G. Markovich, C. P. Collier, S. E. Henrichs, F. Remacle, R. D. Levine and J. R. Heath, *Acc. Chem. Res.*, 1999, **32**, 415.
14 Y. Abbas, F. A. Deader, A. Qurashi, M. Al-Qutayri, V. Chan and M. Rezeq, *Adv. Electron. Mater.*, 2025, **11**, 2400363.
15 A. Yañez-Aulestia, N. K. Gupta, M. Hernández, G. Osorio-Toribio, E. Sánchez-González, A. Guzmán-Vargas, J. L. Rivera, I. A. Ibarra and E. Lima, *Chem. Commun.*, 2022, **58**, 249–270.

16 I. del-Campo, A. Sorroche, N. Allen, M. Ghirardello, F. Corzana, M. Carmen Galán, M. Monge and J. M. López-de-Luzuriaga, *Nanoscale Adv.*, 2025, **7**, 3228.
17 S. Ngernpimai, T. Puangmali, A. Kopwitthaya, P. Tippayawat, A. Chompoosor and S. Teerasong, *ACS Appl. Nano Mater.*, 2024, **7**, 13124–13133.
18 S. Borsley, W. Edwards, I. K. Mati, G. Poss, M. Diez-Castellnou, N. Marro and E. R. Kay, *Chem. Mater.*, 2023, **35**, 6168–6177.
19 Y. Oleksii and A. El-Ghayoury, *Molecules*, 2025, **30**, 1314.
20 Y. S. L. V. Narayana, S. Basak, M. Baumgarten, K. Müllen and R. Chandrasekar, *Adv. Funct. Mater.*, 2013, **23**, 5875–5880.
21 Y. S. L. V. Narayana, D. Venkatakrishnarao, A. Biswas, M. A. Mohiddon, N. Viswanathan and R. Chandrasekar, *ACS Appl. Mater. Interfaces*, 2016, **8**, 952–958.
22 A. K. Botcha, S. Basak and R. Chandrasekar, *RSC Adv.*, 2014, **4**, 34760–34763.
23 P. Gutlich, Y. Garcia and H. A. Goodwin, *Chem. Soc. Rev.*, 2000, **29**, 419–427.
24 S. Basak, P. Hui and R. Chandrasekar, *Chem. Mater.*, 2013, **25**, 3408–3413.
25 N. Chandrasekhar and R. Chandrasekar, *Dalton Trans.*, 2010, **39**, 9872–9878.
26 R. Chandrasekar, O. Fuhr, R. Kruk, M. Ghafari, H. Hahn and M. Ruben, *Chem. Commun.*, 2007, 2636–26384.
27 E. J. Devid, P. N. Martinho, M. V. Kamalakar, U. Prendergast, C. Kubel, T. Lemma, J.-F. Dayen, T. E. Keyes, B. Doudin, M. Ruben and S. J. van der Molen, *Beilstein J. Nanotechnol.*, 2014, **5**, 1664–1674.
28 E. J. Devid, P. N. Martinho, M. V. Kamalakar, I. Salitro, U. Prendergast, J. F. O. Dayen, V. Meded, T. Lemma, R. G. lez-Prieto, F. Evers, T. E. Keyes, M. Ruben, B. Doudin and S. J. van der Molen, *ACS Nano*, 2015, **9**, 4496–4507.
29 M. A. Halcrow, *Chem. Soc. Rev.*, 2011, **40**, 4119–4142.
30 M. A. Halcrow, *Spin Crossover Materials: Properties and Application*, Wiley-Blackwell, Oxford, U.K., 2013.
31 M. A. Halcrow, *Dalton Trans.*, 2024, **53**, 13694–13708.
32 X. Yang, A. Enriquez-Cabrera, K. Jacob, Y. Coppel, L. Salmon and A. Bousseksou, *Dalton Trans.*, 2024, **53**, 6830–6838.
33 J. Yi, E.-M. You, R. Hu, D.-Y. Wu, G.-K. Liu, Z.-L. Yang, H. Zhang, Y. Gu, Y.-H. Wang, X. Wang, H. Ma, Y. Yang, J.-Y. Liu, F. R. Fan, C. Zhan, J.-H. Tian, Y. Qiao, H. Wang, S.-H. Luo, Z.-D. Meng, B.-W. Mao, J.-F. Li, B. Ren, J. Aizpurua, V. A. Apkarian, P. N. Bartlett, J. Baumberg, S. E. J. Bell, A. G. Brolo, L. E. Brus, J. Choo, L. Cui, V. Deckert, K. F. Domke, Z.-C. Dong, S. Duan, K. Faulds, R. Frontiera, N. Halas, C. Haynes, T. Itoh, J. Kneipp, K. Kneipp, E. C. Le Ru, Z.-P. Li, X. Y. Ling, J. Lipkowski, L. M. Liz-Marzán, J.-M. Nam, S. Nie, P. Nordlander, Y. Ozaki, R. Panneerselvam, J. Popp, A. E. Russell, S. Schlücker, Y. Tian, L. Tong, H. Xu, Y. Xu, L. Yang, J. Yao, J. Zhang, Y. Zhang, Y. Zhang, B. Zhao, R. Zenobi, G. C. Schatz, D. Graham and Z.-Q. Tian, *Chem. Soc. Rev.*, 2025, **54**, 1453–1551.
34 H. Ma, S. Q. Pan, W. L. Wang, X. X. Yue, X. H. Xi, S. Yan, D. Y. Wu, X. Wang, G. K. Liu and B. Ren, *ACS Nano*, 2024, **18**, 14000–14019.
35 M. E. Stewart, C. R. Anderton, L. B. Thompson, J. Maria, S. K. Gray, J. A. Rogers and R. G. Nuzzo, *Chem. Rev.*, 2008, **108**, 494–521.
36 S. Basak, M. A. Mohiddon, M. Baumgarten, K. Müllen and R. Chandrasekar, *Sci. Rep.*, 2015, **5**, 8406.
37 U. Venkataramudu, S. Basak, M. A. Mohiddon and R. Chandrasekar, *Chem. Sci.*, 2018, **130**, 77.
38 U. Venkataramudu, N. Chandrasekhar, S. Basak, M. D. Prasad and R. Chandrasekar R, *Macromol. Rapid Commun.*, 2015, **36**, 647.
39 S. Basak, P. Hui, B. Sathyanarayana and R. Chandrasekar, *J. Org. Chem.*, 2012, **77**, 3620–3626.
40 A. Kumar, H. Biebuyck, N. Abbott and G. Whitesides, *J. Am. Chem. Soc.*, 1992, **114**, 9188–9189.
41 A. Kumar and G. M. Whitesides, *Appl. Phys. Lett.*, 1993, **63**, 2002–2004.
42 J. L. Wilbur, A. Kumar, E. Kim and G. M. Whitesides, *Adv. Mater.*, 1994, **6**, 600–604.
43 C. Hanske, E. H. Hill, D. Vila-Liarte, G. González-Rubi, C. Matricardi, A. Mihi and L. M. Liz-Marzán, *ACS Appl. Mater. Interfaces*, 2019, **11**, 11763–11771.
44 K. Deng, Z. Luo, L. Tan and Z. Quan, *Chem. Soc. Rev.*, 2020, **49**, 6002–6038.
45 R. Chandrasekar, F. Shramm, O. Fuhr and M. Ruben, *Eur. J. Inorg. Chem.*, 2008, 4860–4862.
46 P. Crespo, R. Litran, T. C. Rojas, M. Multigner, J. M. De la Fuenta, J. C. Sanchez-Lopez, M. A. Garcia, A. Hernando, S. Penades and A. Fernandez, *Phys. Rev. Lett.*, 2004, **93**, 087204.
47 M. Hasan, D. Bethell and M. Brust, *J. Am. Chem. Soc.*, 2002, **124**, 1132–1133.
48 P. Pramod, P. K. Sudeep, K. G. Thomas and P. V. Kamat, *J. Phys. Chem. B*, 2006, **110**, 42.
49 P. Crespo, R. Litran, T. C. Rojas, M. Multigner, J. M. de la Fuente, J. C. Sánchez-Lopez, M. A. Garcia, A. Hernando, S. Penades and A. Fernandez, *Phys. Rev. Lett.*, 2005, **94**, 049903.
50 M. A. Mohiddon, L. D. V. Sangani and M. G. Krishna, *Chem. Phys. Lett.*, 2013, **588**, 160–166.
51 T. W. Odom, J. C. Love, D. B. Wolfe, K. E. Paul and G. M. Whitesides, *Langmuir*, 2002, **18**, 5315–5320.